Analysis and High-Frequency Model of Three-Phase Four-Wire Common Mode Chokes

Yujie Lan, *Student Member, IEEE*, Wei Chen, *Member, IEEE*, Qing He, and Qingbin Chen

***Abstract*—Common mode chokes (CMCs) are key components in electromagnetic interference (EMI) filters, and accurate modeling of these components is critical for filter design and EMI noise simulation. This article proposes a behavioral model and parameter extraction technique for characterizing three-phase four-wire common mode chokes (4W-CMCs). The proposed model considers the inductance nonlinearity caused by the nonlinear permeability of manganese-zinc ferrite and nanocrystalline magnetic materials, as well as the asymmetry and local symmetry in the winding distribution of 4W-CMCs. The parameters for the common mode and differential mode (DM) models are extracted using a parameter extraction program and a simple equation-based method, respectively. For the DM model parameter extraction, this article proposes a measurement method that utilizes the local symmetry of 4W-CMCs. The equivalent circuit of this measurement method decouples the interwinding capacitance (C_W) from the DM inductance parallel capacitance (C_D) by transforming two-port network parameters, greatly simplifying the parameter extraction process. The accuracy of the model and the effectiveness of the method are validated through experiments using several 4W-CMCs with manganese-zinc ferrite and nanocrystalline magnetic cores.**

***Index Terms*—Common mode chokes (CMCs), electromagnetic interference, filters, model analysis, parasitic parameter extraction.**

I. Introduction

With the development of power electronic devices towards higher power densities, electromagnetic interference (EMI) has become an increasingly critical issue. EMI filters are commonly used to suppress conducted EMI in power electronic devices [1], [2], [3]. Passive filters are frequently chosen in converters due to their high-power handling capacity, cost-effectiveness, stability, and reliability [4], [5], [6].

Common mode chokes (CMCs) are vital components of passive EMI filters, and accurate modeling of these components is fundamental for EMI noise analysis and filter design [7], [8]. Three-phase four-wire common mode chokes (4W-CMCs) are often used in three-phase four-wire converters to suppress conducted EMI. At high frequencies, the nonlinear permeability of the magnetic core, leakage parameters, and parasitic capacitance of the windings make predicting the characteristics of CMCs challenging [9].

Research on high-frequency models of CMCs has been a hot topic in EMI studies [10]. Based on this, Moonen et al. [11] and Bingler et al. [12] utilized the theory of field analysis combined with complex permeability to establish a finite element simulation model for three-phase three-wire common mode chokes (3W-CMCs). This approach can accurately extract internal parasitic parameters and effectively reduce simulation time. Moonen et al. [11] and Heldwein et al. [13] proposed a calculation method for internal parasitic capacitance based on the geometric shape and material parameters of 3W-CMCs and developed a parasitic parameter calculation model based on 3W-CMC structural parameters [14].

Currently, using impedance analyzers or vector network analyzers (VNA) to describe the high-frequency characteristics of common-mode chokes (CMCs) is the most common and efficient method [15], [16]. In higher power applications, such as EV chargers and converters, photovoltaic inverters, and aerospace systems, CMCs typically use manganese-zinc ferrite or nanocrystalline materials [17]. These materials have higher permeability and higher saturation flux density. Due to the stronger frequency nonlinearity of nanocrystalline materials, which leads to a gradual decrease in inductance, and the sharp peak in the permeability of manganese-zinc ferrite that can cause local resonance, fitting the CM components of CMCs becomes more challenging. Recent reports have employed multistage *RC* models to fit the nonlinearity of ferrite materials [18], or *RL* models to fit the nonlinearity of nanocrystalline materials [19] and used particle swarm optimization (PSO) to extract parameters. However, the unclear magnitude of initial values in the iterative process of multistage models can lead the algorithm into local optima.

Compared to common-mode models, studying the differential mode (DM) models of CMCs and 3W-CMCs is more challenging. Kotny et al. [20] developed various CMCs testing methods based on impedance analyzers and established a high-frequency model to characterize the attenuation performance of 2W-CMC under different tests. Tan et al. [21] used an iterative rational function approximation algorithm on the model and testing methods in [20] to extract parameters from the 2W-CMC model. Stevanovic et al. [22] extended the 2W-CMC model to the 3W-CMC, setting the coupling inductance to $k = -1/3$ to counteract its attenuation effect on CM currents, and ultimately employed a genetic algorithm (GA) to obtain a multiresonance point 3W-CMC model. However, using an impedance analyzer

---

Received 2 July 2024; revised 17 October 2024; accepted 15 November 2024. Date of publication 19 November 2024; date of current version 26 December 2024. This work was supported by the Delta Power Electronics Science and Education Development Program of Delta Group. Recommended for publication by Associate Editor H. Li. *(Corresponding author. Qingbin Chen.)*

The authors are with the College of Electrical Engineering and Automation, Fuzhou University, Fuzhou 350108, China (e-mail: 230110006@fzu.edu.cn; chw@fzu.edu.cn; 220120023@fzu.edu.cn; cqb@fzu.edu.cn).

Color versions of one or more figures in this article are available at https://doi.org/10.1109/TPEL.2024.3502224.

Digital Object Identifier 10.1109/TPEL.2024.3502224

or vector network analyzer connected to two terminals while shorting the other two terminals can lead to inaccurate measurements, as it neglects the displacement current variations in the high-frequency magnetic core [23], [24], [25] analyzed the CMC as a four-port device, testing the 2W-CMC in accordance with EN55017 and CISPR-17 using a VNA, and extracted model parameters using a curve-fitting algorithm. Based on this, Domínguez-Palacios et al. [26] extended the model and modeling methods from [25] to the 3W-CMC, treating it as a six-port device, analyzing five non-zero admittance modes in the 3W-CMC, and finally using PSO to extract parasitic parameters. Jie et al. [27] introduced single-port circuit de-embedding and three-port network calibration measurement methods for the 3W-CMC, considering the parasitic effects of fixture adapters.

However, there are significant differences in the modeling methods between 4W-CMCs and 3W-CMCs. Recent research [23] analyzed the lack of symmetry in 4W-CMCs due to spatial positioning and distance differences among the four windings, leading to significant discrepancies in the S21 measurements of the two windings, which were verified in this study. Thus, the 3W-CMCs model ([22], [26]) is difficult to apply directly to 4W-CMCs, as the previous 3W-CMC model based on symmetric arrangements cannot represent the different magnetic coupling characteristics between the windings of 4W-CMCs. Ojeda-Rodríguez et al. [23] proposed a 4W-CMC model to address this issue, where the DM model is divided into two parts that operate differently under DM current excitation in different windings; however, this significantly increases the complexity of the model.

This article proposes a high-frequency model for 4W-CMCs suitable for frequency-dependent magnetic materials based on the 3W-CMC model and a parameter extraction method based on scattering parameter measurements. Compared to the previously reported 3W-CMCs model, the proposed model effectively fits the asymmetry of 4W-CMCs. Additionally, the 4W-CMCs DM model proposed here is much simpler than that in [23], as it differentiates the magnetic coupling capabilities of the 4W-CMCs windings based on the mutual inductance between phases rather than differences in self-inductance. Furthermore, this study presents a testing method for the local symmetry of 4W-CMCs and a parameter extraction method that converts scattering parameters into admittance parameters, allowing accurate model parameters to be obtained using only a few simple linear equations. This approach eliminates the need for testing initial values and debugging procedures associated with earlier numerical iterative methods to achieve more precise values.

The rest of this article is organized as follows. Section I of this article introduces the asymmetry of 4W-CMCs and the testing methods to extract the transmission characteristics of 4W-CMCs under different operating modes. Section II analyzes the modeling of the CM component under the nonlinear effects of the magnetic permeability of frequency-dependent magnetic materials and the GA-based parameter extraction method. Section III establishes the DM model of 4W-CMCs based on its asymmetry and proposes a new testing method and a method for extracting parameters in the DM model based on the conversion of scattering parameters to admittance parameters. Section IV verifies the CM and DM models of 4W-CMCs, both achieving good fitting results. Finally, Section V concludes this article.

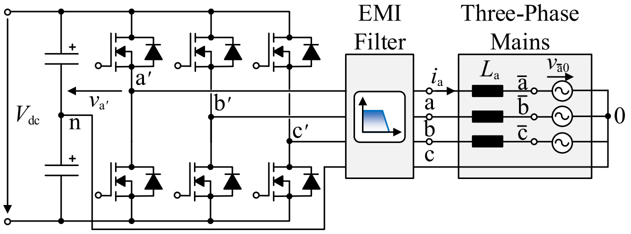

Fig. 1. Three-phase four-wire inverter system.

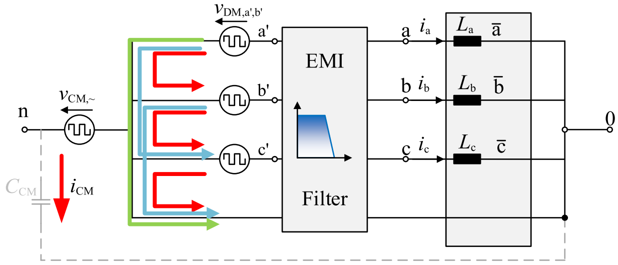

Fig. 2. Noise equivalent circuit of three-phase four-wire system.

II. Model Analysis

A. Analysis of 4W-CMCs System

Fig. 1 shows a three-phase inverter. Since the fundamental frequency components are typically not considered in conducted EMI, only the high frequency switching components need to be considered. The equivalent circuit of the three half-bridges can be simplified to four high-frequency voltage sources, one CM, and three DM voltage sources. The equivalent circuit for EMI noise current is shown in Fig. 2.

Previous studies have distinguished CM and DM in three-phase systems and effectively separated CM and DM noise in asymmetric three-phase systems using the principle of three-phase symmetry [28], [29]. The CM behavior of four-wire systems has been studied in [30]. However, from the perspective of conducted EMI, there is no clear definition of the DM propagation mode in three-phase four-wire systems.

For three-phase four-wire systems, the noise current does not meet the 120° phase shift. According to the definition of CM and DM currents, CM current is the average current on all phase lines and the neutral line, typically considered as current flowing relative to ground, while DM current is considered as the current flowing between phase lines. As shown in Fig. 2, the DM noise current path can be represented as a combination of the DM current paths between six pairs of phases. Therefore, a qualified 3W-CMC and 4W-CMC model should characterize DM attenuation between any two phases. Special attention should be given to the two-phase operating mode of CMCs, as specified by CISPR-17 and EN55017. Therefore, current studies on 3W-CMCs, which focus on attenuation characteristics obtained from DM mode measurements, are not comprehensive enough [22], [23], [26] provides a detailed analysis of the CM and DM behavior in the 4W system, and the testing methods used

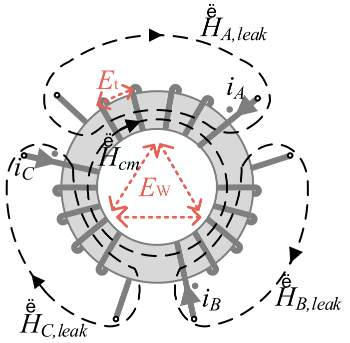

Fig. 3. Electromagnetic field distribution of the 3W-CMC, where the red dashed lines represent the electric field distribution, and the black dashed lines represent the magnetic field distribution.

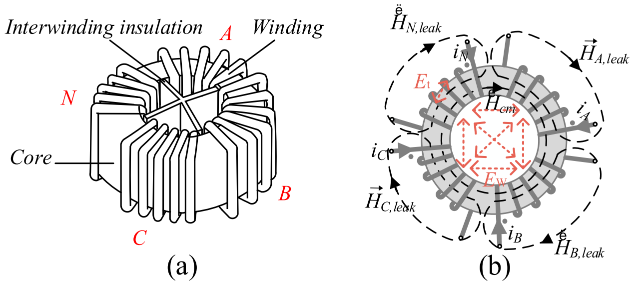

(a) (b)

Fig. 4. Diagram of the 4W-CMC. (a) Schematic of the physical structure of the 4W-CMC. (b) Schematic of the internal electromagnetic field distribution of the 4W-CMC.

in its CMC modeling comply with the CISPR-17 and EN55017 standards. It provides a great perspective for the operation of the 4W system.

B. Asymmetry and Local Symmetry of 4W-CMC

The modeling of 4W-CMC is similar to that of 3W-CMCs, and the modeling work can start with the analysis of 3W-CMCs. The electromagnetic field diagram of 3W-CMCs is shown in Fig. 3. It generates CM components from the main magnetic flux inside the magnetic core and DM components from the leakage flux outside the air gap. Therefore, 3W-CMC suppresses DM currents at high frequencies [31]. A high-frequency model of 3W-CMC should not only describe the internal magnetic field and leakage field responses of the magnetic core at high frequencies but also accurately characterize the electric field response coupled through the magnetic core between winding turns and between windings.

The 3W-CMC is composed of a magnetic core and three identical windings. Due to the equal spacing and structural parameters of any two windings, it forms a symmetrical three-phase structure. Thus, the model of the 3W-CMC should also be symmetrical. In contrast, the 4W-CMC clearly does not possess this characteristic. Fig. 4(a) shows the structure of the 4W-CMC, where the relative positions of any two-phase windings are different, causing variations in leakage parameters. This leads to significant changes in the high-frequency characteristics of the 4W-CMC, which has been demonstrated through testing in the following text. Fig. 4(b) displays the electromagnetic field distribution of the 4W-CMC. EW shows the electric field between the windings, primarily coupled through the near-field electric field of the magnetic core with high dielectric constant. In this case, the core can be considered an equipotential body. To better illustrate the interaction between the windings, the electric field lines are drawn outside the windings. Et shows the electric field distribution caused by the potential difference between turns.

Fig. 5 shows the common setups used for modeling CMC and 3W-CMC. Fig. 5(a) is used to test the suppression capability of the 4W-CMC for CM response. For convenience, the setup shown in Fig. 5(a) is referred to as S_{21}^{CM}. Fig. 5(b) shows the measurement setup according to the CISPR-17 and EN55017 standards. In this work, it is used to extract the DM response parameters of the two-phase windings and for model validation, where the test of phases i and j is referred to as S_{21}^{ij}. Fig. 5(c) is used to extract the DM response parameters of the four-phase windings, with the N phase in series with the ABC three-phase parallel structure (S_{21}^{N}). This structure is used only for model validation. Fig. 5(d) presents the local symmetry connection method based on the 4W-CMC proposed in this article. The two-phase parallel structure of the A and C phases in series with the two-phase parallel structure of the B and N phases ($S_{21}^{\mathrm{AC-BN}}$) significantly reduces the workload of parameter extraction and will be analyzed later. Fig. 5(e) is for extracting the internal winding (IW) parasitic capacitance S_{21}^{IW} setup. In the IW connection, the overall CMC exhibits capacitive behavior, and the response is proportional to the capacitance between the windings. Fig. 5(f) shows the traditional DM testing method. This testing method is similar to the method used by impedance analyzers, where two adjacent terminals are shorted together. However, this results in the displacement current in high dielectric constant cores being different from the DM testing method used in Fig. 5(b), as specified by EN55017 [23]. The differences between the two methods will be illustrated in Fig. 6.

It is worth mentioning that the S_{21}^{ij} and $S_{21}^{\mathrm{AC-BN}}$ tests require the use of RF transformers for auxiliary testing. RF transformers have parasitic capacitance or leakage inductance; However, for bandwidth transformers, the leakage inductance and parasitic capacitance are typically very small. We usually include the RF transformer in the calibration of the VNA to facilitate the calibration of the effects of the parasitic parameters of the RF transformer.

Fig. 6 shows the comparison results of S_{21}^{AN}, S_{21}^{BN}, and S_{21}^{CN} through three different tests conducted on S_{21}^{ij}, as illustrated in Fig. 5(c).

Fig. 6 shows that the characteristics of S_{21}^{AN} and S_{21}^{BN} differ significantly in the 100 kHz to 30 MHz range. The primary reason for the difference between S_{21}^{AN} and S_{21}^{BN} can be attributed to the greater distance between phase B and phase N compared to the distance between phase A and phase N, while the distance between phase A and phase B is equal to the distance between phase A and phase N. This structural difference leads to varying magnetic coupling between the phases, ultimately resulting in differences in the S-parameters during two-phase testing. This is considered a challenge in DM modeling for 4W-CMC. This results in M_{AC} being less than M_{AB}. On the other hand, S_{21}^{AN}

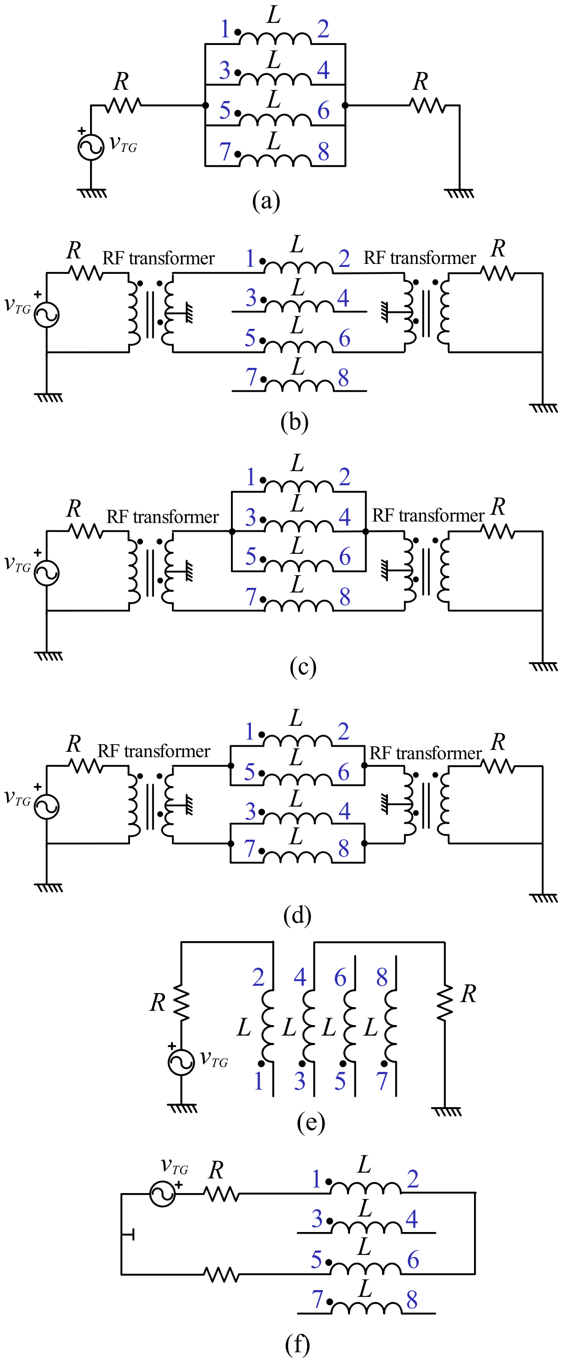

Fig. 5. Insertion loss test setups used in this article. (a) CM configuration. (b) DM configuration according to the CISPR-17 standard. (c) DM extraction setup from [20]. (d) Proposed DM extraction setup in this paper. (e) Parasitic capacitance extraction between windings. (f) DM configuration that does not comply with the CISPR-17 standard.

and S_{21}^{CN} exhibit similar magnetic and electric field responses due to the approximately equal distances between phase A and the N and phase C and N, a phenomenon we refer to as the local symmetry of 4W-CMC.

Based on this, some mutual inductance approximations can be made $M_{\mathrm{AC}} = M_{\mathrm{BN}}$, and $M_{\mathrm{AB}} = M_{\mathrm{AN}} = M_{\mathrm{BC}} = M_{\mathrm{CN}}$. These approximations can effectively simplify the complex equivalent circuit in Section III.

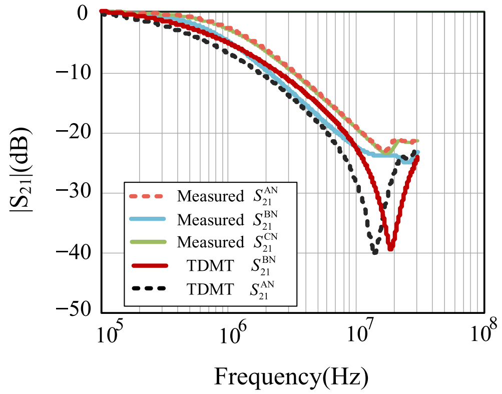

Fig. 6. Comparison of test results between the S_{21}^{ij} setup and the traditional DM testing setup under the close-distance winding AN and the far-distance winding BN.

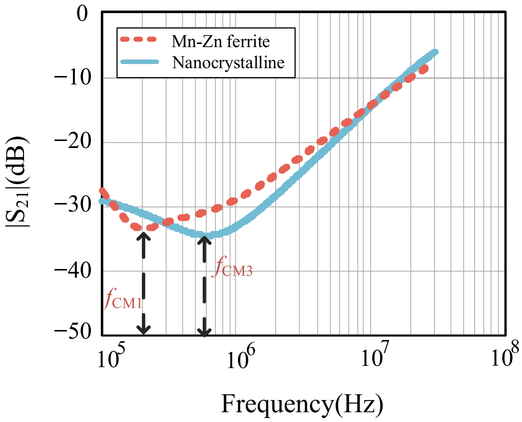

Fig. 7. Comparison of the amplitude of the CM component of S_{21} between the common-mode choke using nanocrystalline and Mn-Zn ferrite materials.

C. Nonlinearity of Permeability in Frequency-Dependent Materials

The core materials with frequency dependence primarily used for CMCs are manganese-zinc ferrite and nanocrystalline materials. The strong frequency dependence of high-permeability manganese-zinc ferrite mainly stems from the frequency response characteristics of its permeability. As frequency increases, the real part of the permeability drops significantly, while the imaginary part rises, leading to a peak in the permeability magnitude at a certain frequency (f_{CM1}). The frequency dependence of nanocrystalline materials is different, as their permeability decreases gradually over a broader frequency range without a distinct peak. This is because nanocrystalline materials have a more uniform microstructure, and the domain wall motion and eddy current effects are relatively weaker at high frequencies, resulting in a smoother frequency response.

Figs. 7 and 8 show the magnitude and phase of the CM impedance curves for nanocrystalline and manganese-zinc ferrite materials. f_{CM1} corresponds to the impedance peak of

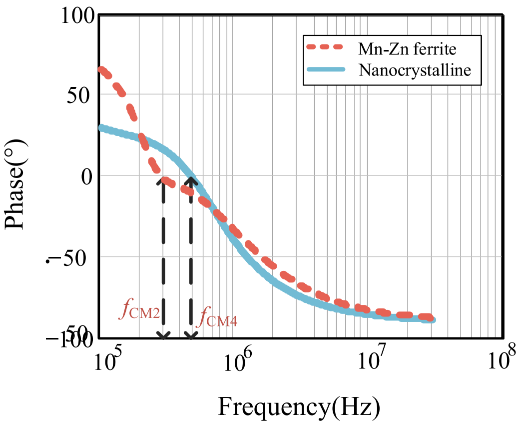

Fig. 8. Comparison of the phase of the CM component of S_{21} between the common-mode choke using nanocrystalline and Mn-Zn ferrite materials.

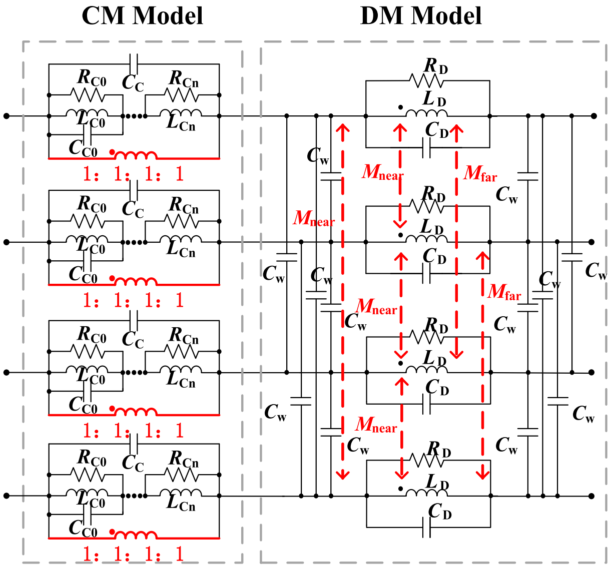

Fig. 9. Circuit model of the 4W-CMC for frequency-dependent materials. The CM model is characterized by a series *RL* parallel model to represent the nonlinearity of permeability. The DM model uses an LCR resonant circuit to model each winding. M_{near} and M_{far} represent the magnetic coupling between adjacent and distant windings, respectively.

manganese-zinc ferrite, f_{CM2} corresponds to the phase zero-crossing point of manganese-zinc ferrite, f_{CM3} corresponds to the impedance peak of nanocrystalline materials, and f_{CM4} corresponds to the phase zero-crossing point of nanocrystalline materials.

In Figs. 7 and 8, it can be observed that the CM impedance trends caused by the two materials are different: manganese-zinc ferrite shows a peak at the magnitude of permeability (f_{CM1}), while the inductance of nanocrystalline material gradually decreases. A common feature of both materials is that the maximum value of the CM impedance magnitude and the phase zero-crossing point do not coincide, which cannot be accurately fitted using a simple parallel *RLC* model.

Based on the abovementioned analysis, a new high-frequency model for the 4W-CMC is proposed, as shown in Fig. 9. The CM part of the 4W-CMC model employs a multi-stage *RL* parallel structure to fit the nonlinear permeability and loss characteristics of the material. In the first stage of the *RL* parallel structure, an additional resonant capacitor C_{C0} is introduced, which resonates with part of the CM inductance to quickly fit the local resonance point of the CM insertion loss for manganese-zinc ferrite. When fitting the CMC of nanocrystalline material, the model does not need to be changed; simply setting $C_{\mathrm{C0}} = 0$ allows for accurate fitting. In the DM part, the issue of differing winding magnetic coupling structures in existing 2W-CMC [20], [21] and 3W-CMC [22], [26] models, which are not applicable to the 4W-CMC, is addressed by setting different coupling inductances. Compared to the latest models from existing research [23], the proposed model achieves significant simplification while realizing different winding magnetic couplings.

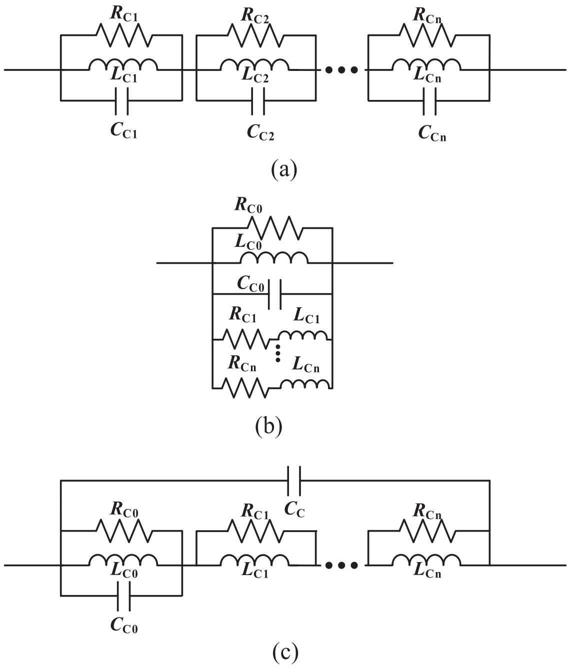

Fig. 10. CM model of CMC made of Frequency-dependent permeability nonlinear material. (a) Traditional multi-stage parallel *RLC* model. (b) Proposed CM model in this [19]. (c) Proposed CM model in this paper, where a series *RL* parallel model represents the frequency nonlinearity of the magnetic core.

III. HIGH-FREQUENCY MODEL CM PARAMETER EXTRACTION FOR 4W-CMC

A. *CM Component Model*

From the discussion in Section II, it is clear that fitting the impedance nonlinearity induced by frequency-dependent magnetic materials with an *RLC* parallel model is challenging. The circuit model of 4W-CMC shown in Fig. 9 can be divided into two distinct circuit modules, the CM module, which explains the response of 4W-CMC to CM excitation, and the four windings configured as a 1:1 transformer to ensure no attenuation effect on DM excitation.

The CMC of frequency-dependent permeability nonlinear materials is typically represented by a multistage parallel *RLC* model to characterize the strong nonlinearity of the material. Fig. 10(a) shows one commonly used type. However, traditional

CM models for CMC have two problems: the parasitic capacitance between windings is not clearly defined, and it is difficult to obtain accurate initial values for algorithm iteration. In traditional models, C_{C1} is only used to fit the decline in permeability, and the model cannot clearly represent the effects of interturn capacitance and the interactions between the windings and the magnetic core. Additionally, obtaining accurate initial values for iteration is challenging. After the first resonance peak, the second-stage *RLC* parallel model fits the characteristics, but after the resonance peak, it can only rely on algorithmic searches for possible values, which poses a significant challenge to numerical computation methods.

Ojeda-Rodríguez et al. [19] proposed an optimized CM module [as shown in Fig. 10(b)] that uses the *RL* admittance function of the Foster II circuit. In [19]'s model, obtaining initial values remains an issue, as C_{C0} and R_{C0} are extracted based on the resonance point f_{CM2}, and parallel *RL* series branches are used to characterize the frequency nonlinearity of the magnetic core beyond the resonance point. However, obtaining effective initial values for the *RL* series branches is difficult. And when fitting ferrite materials, the model needs to be changed to an *RC* series model [18].

Therefore, this article proposes an optimized model that allows for easier acquisition of initial values over a wider frequency range. By incorporating additional resonant capacitance, it can more effectively fit the attenuation characteristics of the peak points and resonance points of manganese-zinc ferrite. Moreover, this model can also be used to fit the characteristics of nanocrystalline materials by simply setting the resonant capacitance to zero.

The proposed model for fitting the permeability nonlinearity is shown in Fig. 10(c). The impedance of the CM model can be expressed as (1), where N_{C} is the number of stages in the *RL* parallel model, $L_{\mathrm{C}n}$ is the CM inductance of the *n*th stage, and $R_{\mathrm{C}n}$ is the loss resistance of the *n*th stage. The relationship between the CM impedance Z_{CM} and the transfer coefficient magnitude $|S_{21}|$ can be expressed as (2)

$$Z_{\mathrm{CM}} = \left(\left(\frac{\mathrm{j}\omega R_{\mathrm{C0}} L_{\mathrm{C0}}}{R_{\mathrm{C0}} - 2\omega^2 R_{\mathrm{C0}} L_{\mathrm{C0}} C_{\mathrm{C0}} + 2\mathrm{j}\omega L_{\mathrm{C0}}} + \sum_{\mathrm{n}=1}^{N_C} \frac{R_{\mathrm{Cn}} \cdot \mathrm{j}\omega L_{\mathrm{Cn}}}{R_{\mathrm{Cn}} + \mathrm{j}\omega L_{\mathrm{Cn}}}\right)^{-1} + \mathrm{j}\omega C_{\mathrm{C}}\right)^{-1} \tag{1}$$

$$\left|S_{21}^{\mathrm{CM}}\right| = 20\,\mathrm{lg}\left(\left|\frac{2R}{2R + Z_{\mathrm{CM}}}\right|\right). \tag{2}$$

The model defines the C_{C} as the lumped parasitic capacitance between CMC windings and between the magnetic core and windings. The resonant capacitor C_{C0} is used to resonate with part of the common-mode inductance L_{C0} to fit the local resonance point (f_{CM1}) caused by the peak of the permeability magnitude of the ferrite material. L_{C0}, C_{C0}, and R_{C0} are configured in parallel to characterize the nonlinear inductance caused by the nonlinearity of the permeability. The n-stage *RL* parallel branches aim to explain the nonlinear behavior and losses of the permeability in the core. It is worth noting that the inductive nonlinearity of nanocrystalline materials results from the slow decline of permeability rather than a peak. Therefore, in the fitting of nanocrystalline materials, C_{C0} is removed from the model, and only the multistage *RL* parallel configuration is used to fit the trend of inductance decline.

Since the model treats C_{C} as the parasitic capacitance of the CMC, and the high-frequency response is primarily dominated by the electric field of C_{C}, an approximate value of C_{C} in the CMC, $C_{\mathrm{CW\_IN}}$, can be extracted at high frequencies based on the calculation formula for the winding parasitic capacitance (3). In (3), $C_{\mathrm{CW\_IN}}$ is the parallel combination of the insulation layer capacitance $C_{\mathrm{tt,\ ins}}$ and the air gap capacitance $C_{\mathrm{tt,\ air}}$ [32], [33]

$$\begin{cases} C_{\mathrm{tt,ins}} = \int_0^{\theta_1} \frac{2\varepsilon_0 \varepsilon_{\mathrm{r}} l_{\mathrm{w}} \mathrm{d}\theta}{\sqrt{\left(\frac{D_{\mathrm{O}}}{2D_{\mathrm{c}}}\right)^2 - \frac{\sin^2\theta}{4} - \frac{\cos\theta}{2}}} + \int_{\theta_1}^{\theta_{\mathrm{m}}} \frac{2\varepsilon_0 \varepsilon_{\mathrm{r}} l_{\mathrm{w}} \mathrm{d}\theta}{\ln\left(\frac{D_{\mathrm{O}}}{D_{\mathrm{c}}}\right)} \\ C_{\mathrm{tt,air}} = \int_0^{\theta_1} \frac{\varepsilon_0 l_{\mathrm{w}} \mathrm{d}\theta}{2(1-\cos\theta)} + \int_{\theta_1}^{\theta_{\mathrm{m}}} \frac{\varepsilon_0 l_{\mathrm{w}} \mathrm{d}\theta}{2\theta \tan\left(\frac{\theta}{2}\right)} \\ C_{\mathrm{CW\_IN}} = 1.366 \frac{C_{\mathrm{tt,ins}} \cdot C_{\mathrm{tt,air}}}{C_{\mathrm{tt,ins}} + C_{\mathrm{tt,air}}} \end{cases} \tag{3}$$

where $\theta_m = \pi/2$, l_w is the length of the winding, D_{o} is the outer diameter of the circular conductor, D_{c} is the inner diameter, ε_0 is the vacuum permittivity, and ε_{r} is the relative permittivity.

The low-frequency response is primarily dominated by the magnetic field response of the series combination of L_{C0} and L_{C1}. In the model, L_{C0} and L_{C1} should have the same order of magnitude; otherwise, a small inductance may be approximated as a short circuit by the larger inductance in series at the lower frequency fcm1, showing inductive characteristics only at higher frequencies. Therefore, when determining the initial iteration values, we set $L_{\mathrm{C0}} = L_{\mathrm{C1}} = L_{\mathrm{CM}}$ /2, as shown in (4), where f_0 represents the lower frequency, typically around 100 kHz or lower in the inductive region

$$L_{\mathrm{C0}} = L_{\mathrm{C1}} = \frac{|Z_{\mathrm{CM}}(f_0)|}{4\pi f_0}. \tag{4}$$

In the interval between f_{CM1} and f_{CM2}, although the parallel structure of L_{C0}, C_{C0}, and R_{C0} has already resonated, the overall phase still exhibits inductive behavior due to the presence of the subsequent L_{C2} level. At time f_{CM2}, the entire Z_{CM} resonates, and the phase is zero, with R_{C2} considered to represent the magnitude of impedance at f_{CM2}. After f_{CM2}, the overall response becomes capacitive, dominated by C_{C}.

Although the above values are not the precise values of the model parameters, the steps outlined provide the GA with relatively accurate initial iteration values to enhance the convergence of the algorithm.

B. Extraction of Parameters in the CM Model.

It is worth mentioning that the CM model only needs to focus on the impedance modeling of a single mode, while all three models can adequately characterize the CM attenuation performance when the order is sufficiently high. The model proposed in this article aims to facilitate the acquisition of iterative initial values and enhance the algorithm's convergence speed at f_{CM1} and f_{CM2}. Accurately determining these values through simple measurement is challenging, which is why GA mechanisms have been developed. However, using GA to fit the CM model still requires some analysis and considerations

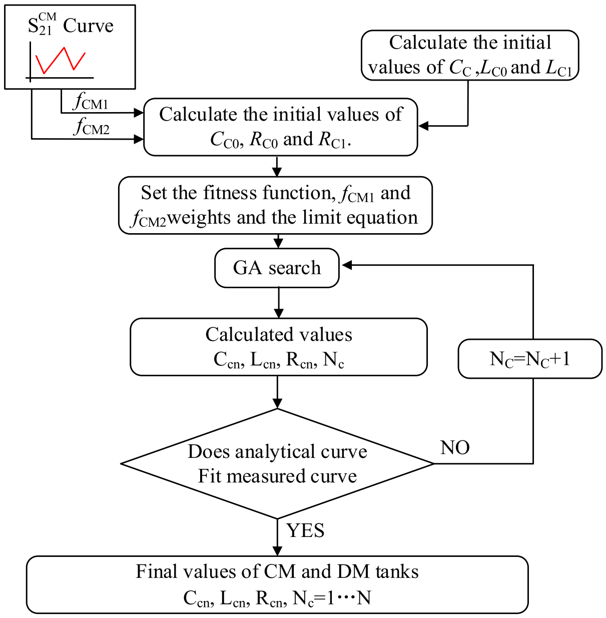

Fig. 11. Flowchart of GA algorithm application in the CM model of a CMC made of frequency-dependent magnetic materials, used for extracting parameters in the CM model.

TABLE I
KEY PARAMETERS FOR GA-BASED MODEL FITTING

Parameter	Typica value
Lower bound for initial population parameters	0.001
Upper bound for initial population parameters	1000
Weight for nonresonance points	1.5
Weight for specific frequency points	5
Mutation rate	3
Maximum number of iterations	100
Number of selected best individuals after genetic screening	200

to shorten computation time and improve result accuracy. The optimized GA extraction process can be illustrated, as shown in Fig. 11, with key GA parameter settings outlined in Table I. First, the impedance curve of the CM is fitted using (1) as the objective function, while (3) and (4) are utilized to calculate the iterative initial values for C_{C}, L_{C1}, and L_{C2}. Then, C_{C0} and R_{C0} are computed based on the local resonance f_{CM1}, and R_{C1} is calculated at the resonance point f_{CM2}. However, in the case of nanocrystalline materials, C_{C0} is set to 0, and R_{C0} and R_{C1} are set to the amplitude at f_{CM2}.The GA evolves the population in each generation through operations such as selection, crossover, and mutation, meaning that each iteration influences the results.

This randomness can help the algorithm escape local optima, but it also means that multiple runs are needed to find better solutions. Therefore, subsequent runs of the algorithm are necessary to select the optimal solution. When the fitting results are unsatisfactory, it may be wise to increase the model order $\mathrm{N_C}$, as typically, a first-order *RL* parallel model is sufficient to fit the flat trend between fcm1 and the phase zero point in the fitting of manganese-zinc ferrite, whereas a second-order model is often required in the fitting of nanocrystalline materials to capture the slow decline in inductance. Additionally, there are some important considerations during the iteration process.

1) Set upper and lower limits for the parameters when searching for unknowns (e.g., the parasitic capacitance of the winding C_{C} ranges from 1 pF to 1 μF, and the inductance ranges from 10 nH to 5 mH). Limiting the effective range of each variable will lead to a more realistic equivalent circuit and significantly reduce the GA search space.
2) Since the curve caused by frequency-dependent magnetic materials typically has only one impedance peak, assigning greater weights to the impedance peak points and phase zero-crossing points can significantly improve the convergence of GA, achieving a global optimal solution. According to Table I, during the iteration process, the frequency points at the impedance peak and the phase zero-crossing points are read out, and a weight of 5 is assigned to these two points, while weights of 1.5 are assigned to points outside of these.
3) When the second-order model is difficult to fit, select the best-performing second-order model parameters as the initial values for the third-order model to reduce the computation process of GA.

IV. HIGH-FREQUENCY MODEL DM PARAMETER EXTRACTION FOR 4W-CMC

A. DM Component Model

In the modeling of CMCs, it is essential to ensure that the CM model approximates a short circuit under DM excitation, and vice versa. This ensures that the CM and DM models can be separately modeled without mutual interference. The typical approach is to set the CM model as a coupled inductor with a coupling factor $\mathrm{k} = 1$ or as a transformer with a turn's ratio $\mathrm{n} = 1$. For single-phase CMCs, the DM model is set as a coupled inductor with $\mathrm{k} = -1$ [as shown in Fig. 12(a)]. In the case of 3W-CMC, the DM model is set as a coupled inductor with $\mathrm{k} = -1/2$ [as shown in Fig. 12(b)] [20], [23], [24]. The mutual inductance of the DM model in this setup is necessary to explain the absence of DM resonance at high frequencies in the S_{21}^{CM} setup.

Similarly, for 4W-CMC, the coupling factor should be set to $\mathrm{k} = -1/3$ to eliminate the response to CM currents. However, Fig. 6 has already validated that 4W-CMC exhibit significant asymmetry compared to 3W-CMC. In 4W-CMC, if the winding method for each phase is identical, the inductance of the DM components can be assumed to be $L_{\mathrm{DA}} = L_{\mathrm{DB}} = L_{\mathrm{DC}} = L_{\mathrm{DN}} = L_{\mathrm{D}}$. In this case, setting the coupling factor k uniformly to $-1/3$ fails to reflect the spatial arrangement asymmetry of the windings. Therefore, to characterize the different magnetic couplings of the various windings, without loss of generality, the i, j windings should be set as coupled inductors with mutual inductance $M = M_{\mathrm{ij}}$ [as shown in Fig. 12(c)].

Under the excitation of CM currents, the DM model is shown in Fig. 13. At this time, the voltage drops $V_{\mathrm{DM\_A}}$ across phase A in the DM model is given by (5). To maintain the characteristic of the model approximating a short circuit under CM currents,

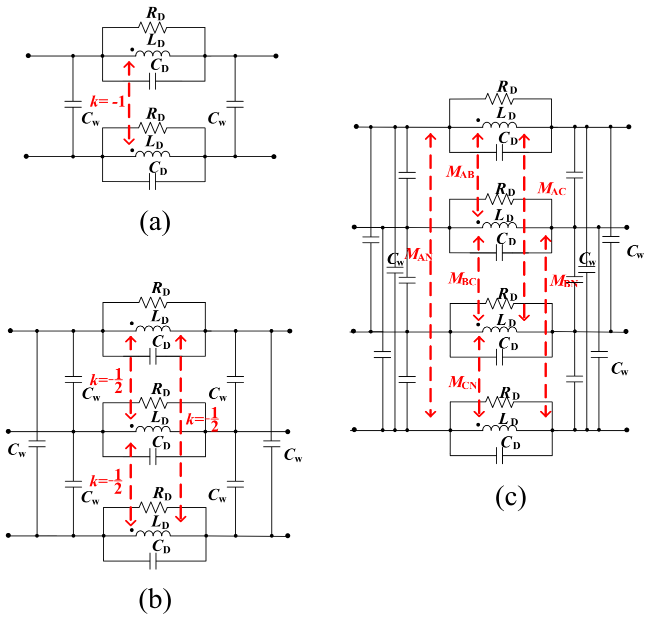

(a)

(b)

(c)

Fig. 12. Equivalent circuit model of CMC DM component. (a) 2W-CMC. (b) 3W-CMC. (c) 4W-CMC.

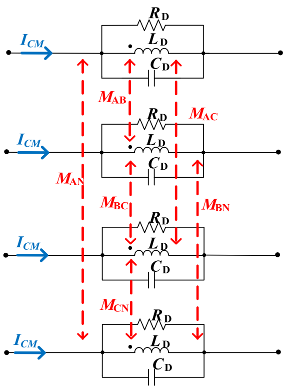

Fig. 13. Equivalent circuit of the DM component of the 4W-CMC under common-mode excitation, which exhibits a short-circuit characteristic for CM excitation.

it must satisfy (6). Extending this to any phase, we obtain (7). Based on this mutual inductance cancellation mechanism, the mutual inductance of the other three phases can offset the decay of CM currents caused by the DM inductance L_{D} in one phase

$$\begin{aligned}\dot{V}_{\mathrm{DM\_A}} &= \mathrm{j}\omega L_{\mathrm{D}} \cdot \dot{I}_{\mathrm{CM}} + \mathrm{j}\omega\left(M_{\mathrm{AB}} + M_{\mathrm{AC}} + M_{\mathrm{AN}}\right) \cdot \dot{I}_{\mathrm{CM}} \\ &= \mathrm{j}\omega \dot{I}_{\mathrm{CM}} \cdot \left(L_{\mathrm{D}} + M_{\mathrm{AB}} + M_{\mathrm{AC}} + M_{\mathrm{AN}}\right)\end{aligned} \tag{5}$$

$$L_D + M_{AB} + M_{AC} + M_{AN} = 0 \tag{6}$$

$$\begin{aligned}&M_{AB} + M_{AC} + M_{AN} \\ &= M_{AB} + M_{BC} + M_{BN} \\ &= M_{AC} + M_{BC} + M_{CN} \\ &= M_{AN} + M_{BN} + M_{CN}.\end{aligned} \tag{7}$$

Based on the local symmetry of the 4W-CMC described in the previous section, the magnetic coupling between two phases at the same distance is also the same. Therefore, we have $M_{\mathrm{AC}} = M_{\mathrm{BN}} = M_{\mathrm{far}}$, $M_{\mathrm{AB}} = M_{\mathrm{AN}} = M_{\mathrm{BC}} = M_{\mathrm{CN}} = M_{\mathrm{near}}$, the parameters can be simplified to three: L_{D}, M_{far}, and M_{near}. Therefore, in the DM model proposed in this article, there are a total of four self-inductances L_{D} and six mutual inductances M (two M_{far} and four M_{near}), which offers significant simplification compared to the 12 self-inductances and 18 mutual inductances in the 4W-CMC model presented in [26].

B. Extraction of Parameters in the DM Model.

This is represented by three different parameters: L_{D}, M_{far}, and M_{near}, which describe the magnetic coupling of the 4W-CMC. Therefore, three different equations related to magnetic field excitation are required to solve these parameters. In the S_{21}^{ij} setup, there are six possible connection methods, which can essentially be categorized into two types, S_{21}^{AN}andS_{21}^{BN}. $S_{21}^{\mathrm{AN}}$is used to test the DM performance between two phases at close range, while S_{21}^{BN} is used to test the DM performance between two phases at a greater distance.

Taking S_{21}^{AN}as an example, at low frequencies, the coupling effects of the magnetic and electric fields of phases B and C can be ignored. This is because the parasitic capacitance C_{w} between the windings is typically only a few pF, while the DM equivalent resistance R_{D} can reach several kΩ, approximating an open circuit at low frequencies. The impedance S_{21}^{AN} at low frequencies can be described by the self-inductance and the mutual inductance between A and N, as described by (8). It is important to note that this impedance expression is only applicable to the magnetic field response in the low-frequency range. The accuracy of this expression will be affected by the electric and magnetic field influences of the other two-phase windings above a few MHz.

In the S_{21}^{AN}andS_{21}^{BN} modes, due to magnetic coupling in the measured phase, circulating currents are generated in the open phase through L_{D} and C_{D}, or displacement currents are produced through electric field coupling in the open phase. Therefore, at high frequencies, it becomes difficult to effectively extract C_{D} and R_{D}. The figure below shows a comparison between the simulation of S_{21}^{AN} with and without considering the electric and magnetic field coupling of the open phase (where M and C_{W} of the open phase are set to 0). From the comparison in Fig. 14, it can be seen that while both simulations match before 20 MHz, they diverge after 20 MHz.

Therefore, the third set of tests should avoid having the open phase coupled to the test phase through electric and magnetic fields, which makes it difficult to extract C_{D} and R_{D}. It is preferable to choose a mode where all four phases operate simultaneously

$$2L_D - 2M_{\mathrm{ij}} = \frac{|Z_{\mathrm{ij}}|}{2\pi f_0}. \tag{8}$$

Combining the setup in Fig. 5(b) with the definition of S_{21}^{ij} in (2), the expression for the equivalent impedance $|Z_{\mathrm{ij}}|$ can be derived as

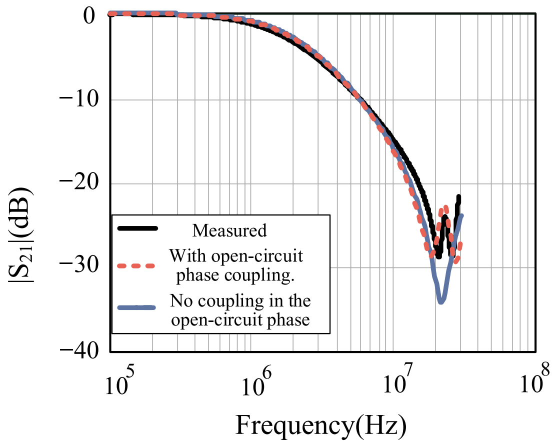

Fig. 14. Simulation comparison of S_{21}^{AN} configuration with and without open-circuit phase effects. In the simulation without open-circuit phase coupling, the mutual inductance (M) and capacitance to winding (C_{W}) of the open circuit phase are set to 0.

$$|Z_{\mathrm{ij}}| = \sqrt{10^{\frac{40-S_{21}^{\mathrm{ij}}}{10}} - 10^4}. \tag{9}$$

S_{21}^{AN} and S_{21}^{BN} have provided two different tests to obtain the magnetic field response of the 4W-CMC. According to the analysis, an additional test is needed to solve for the three unknowns. However, the testing methods used in [21] and [22] extended to 4W-CMC also fail to effectively extract C_{D} and R_{D}. At this point, the currents in phases A, B, and C differ from the current in phase N, resulting in a complex magnetic coupling structure that cannot be simplified into a simple parallel *RLC* circuit (unlike the 3W-CMC). The asymmetry of the 4W-CMC leads to different mutual inductances, which complicates the inductance expressions and prevents the straightforward extraction of C_{D} and R_{D} through series or parallel connections. The equivalent circuit of S_{21}^{N} can be seen in Fig. 15(a).

Therefore, the $S_{21}^{\mathrm{AC-BN}}$ developed in this article, utilizing the local symmetry of the 4W-CMC, is considered an optimized testing method. It not only allows for the simultaneous measurement of the performance of all four phase windings, but also ensures that the current flowing through each phase is the same. The current phase of phase AC is identical, and it is 180° out of phase with phase BC. Furthermore, the magnetic coupling structure can be simplified into an identical expression using (6). Additionally, under DM excitation, $S_{21}^{\mathrm{AC-BN}}$ leverages the local symmetry of the 4W-CMC and the conversion between the scattering matrix and the admittance matrix to achieve the decoupling of C_{W} and C_{D}, greatly simplifying the parameter extraction process and offering significant advantages over $S_{21}^{\mathrm{AC-BN}}$.

The equivalent circuit for $S_{21}^{\mathrm{AC-BN}}$ can be shown in Fig. 15(a). Based on the relationships $M_{\mathrm{AC}} = M_{\mathrm{BN}} = M_{\mathrm{far}}$, $M_{\mathrm{AB}} = M_{\mathrm{AN}} = M_{\mathrm{BC}} = M_{\mathrm{CN}} = M_{\mathrm{near}}$, and incorporating (7) into Fig. 15(b), the circuit can be further simplified to Fig. 15(c).

For the circuit in Fig. 15(c), the two-port S-parameter matrix can be directly converted into various types of two-port matrices. Using (10) and (11), the S-parameters can be converted into Y-parameters

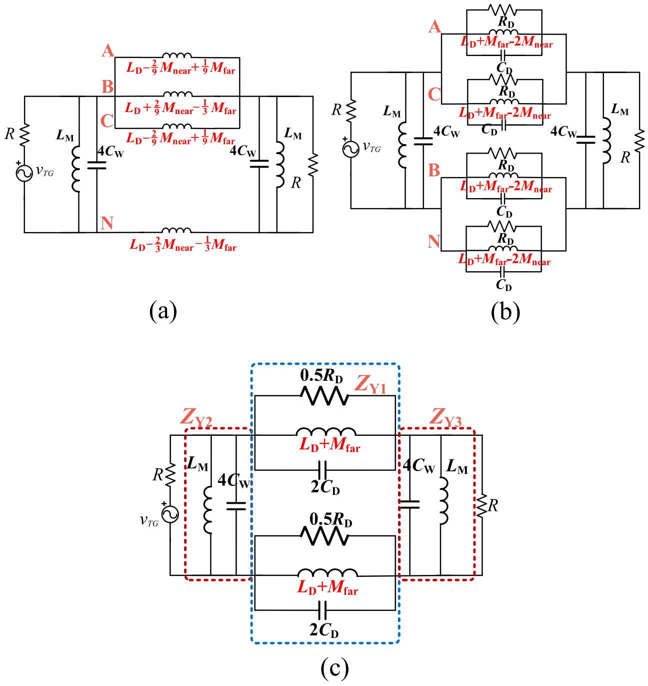

(a) (b) (c)

Fig. 15. Equivalent circuit of DM model under $S_{21}^{\mathrm{AC-BN}}$ and S_{21}^{N} setup. (a) Equivalent circuit in the S_{21}^{N} setup. (b) Equivalent circuit under $S_{21}^{\mathrm{AC-BN}}$. (c) Equivalent circuit under $S_{21}^{\mathrm{AC-BN}}$ simplified through mutual inductance.

$$\begin{cases} Y_{11} = \frac{1}{Z_0}\frac{(1-S_{11})(1+S_{22})+S_{12}S_{21}}{(1+S_{11})(1+S_{22})-S_{12}S_{21}} \\ Y_{12} = \frac{1}{Z_0}\frac{-2S_{12}}{(1+S_{11})(1+S_{22})-S_{12}S_{21}} \\ Y_{21} = \frac{1}{Z_0}\frac{-2S_{21}}{(1+S_{11})(1+S_{22})-S_{12}S_{21}} \\ Y_{12} = \frac{1}{Z_0}\frac{(1+S_{11})(1-S_{22})+S_{12}S_{21}}{(1+S_{11})(1+S_{22})-S_{12}S_{21}}. \end{cases} \tag{10}$$

In this equation: $\mathrm{S_{ii}}$ is the transmission coefficient in the scattering matrix. $\mathrm{S_{ij}}$ is the reflection coefficient in the scattering matrix. After converting the S-parameter matrix into the Y-parameter matrix, the admittance parameters Y_1、Y_2, and Y_3 of the π-type circuit can be obtained. From these, the specific *RLC* parameters of each admittance branch can be calculated

$$\begin{cases} Z_{Y1} = \frac{1}{-Y_{12}} \\ Z_{Y2} = \frac{1}{Y_{11}+Y_{12}} \\ Z_{Y3} = \frac{1}{Y_{22}+Y_{12}}. \end{cases} \tag{11}$$

It is worth noting that at this point, the decoupling of C_{W} and C_{D} has been achieved, because C_{D} exists only in $\mathrm{Z_{Y1}}$, while C_{W} exists only in $\mathrm{Z_{Y2}}$ or $\mathrm{Z_{Y3}}$. In this context, $\mathrm{Z_{Y1}}$ can be represented as a parallel structure of R_{D}, $2(L_{\mathrm{D}}+M_{\mathrm{far}})$ and C_{D}. Both $\mathrm{Z_{Y2}}$ and $\mathrm{Z_{Y3}}$ are the parallel combination of the excitation inductance and parasitic capacitance of the *RF* transformer. This article focuses solely on $\mathrm{Z_{Y1}}$, whose impedance can be expressed as

$$Z_{Y1} = \frac{2\mathrm{j}\omega R_{\mathrm{D}}\left(L_{\mathrm{D}}+M_{\mathrm{far}}\right)}{R_{\mathrm{D}} - 4\omega^2 R_{\mathrm{D}}\left(L_{\mathrm{D}}+M_{\mathrm{far}}\right) + 4\mathrm{j}\omega\left(L_{\mathrm{D}}+M_{\mathrm{far}}\right)}. \tag{12}$$

From (12), the inductance at low frequencies can be derived. Furthermore, the values of C_{D} and R_{D} can be obtained from (13)

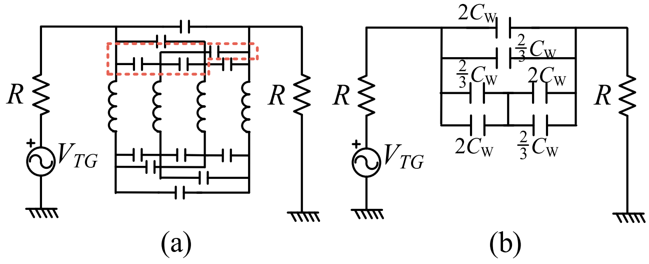

Fig. 16. Equivalent circuit under S_{21}^{IW} setup. (a) Schematic of the interwinding capacitance C_{w} in the S_{21}^{IW} setup. (b) Equivalent circuit obtained through star-delta transformation, neglecting magnetic field effects at low frequencies.

and (14), where f_{ZY1} is the resonance point of $\mathrm{Z_{Y1}}$

$$2L_{\mathrm{D}} + 2M_{\mathrm{far}} = \frac{|Z_{\mathrm{Y1}}|}{2\pi f_0} \tag{13}$$

$$C_{\mathrm{D}} = \frac{1}{(2\pi f_{\mathrm{ZY1}})^2 \cdot 2\left(L_{\mathrm{D}} + M_{\mathrm{far}}\right)} \tag{14}$$

$$R_{\mathrm{D}} = |Z_{\mathrm{Y1}}(f_{\mathrm{ZY1}})| \,. \tag{15}$$

Based on (8) and (13), the magnetic field response parameters can be directly obtained and summarized as (16). Therefore, using (16), the data obtained from the three sets of tests can be directly processed through simple calculations to determine L_{D}, M_{far} and M_{near}. Similarly, the S_{21}^{ij} and S_{21}^{N} tests can also be used for modeling the 3W-CMC.

It is worth mentioning that the $S_{21}^{\mathrm{AC-BN}}$ method requires obtaining $\mathrm{S_{11}}$, $\mathrm{S_{12}}$, $\mathrm{S_{21}}$, and $\mathrm{S_{22}}$, and then converting the S-parameters to Y-parameters, ultimately deriving $\mathrm{Z_{Y1}}$ to jointly extract L_{D}, M_{far}, and M_{near} along with S_{21}^{AN} andS_{21}^{BN}. However, since the $\mathrm{S_{11}}$, $\mathrm{S_{12}}$, $\mathrm{S_{21}}$, and $\mathrm{S_{22}}$, measurements from the VNA are obtained simultaneously, this does not add any additional testing procedures

$$\begin{cases} L_{\mathrm{D}} = \frac{|Z_{\mathrm{Y2}}|+|Z_{\mathrm{far}}|}{8\pi f_0} \\ M_{\mathrm{near}} = \frac{|Z_{\mathrm{Y2}}|-|Z_{\mathrm{near}}|}{8\pi f_0} \\ M_{\mathrm{far}} = \frac{|Z_{\mathrm{Y2}}|-|Z_{\mathrm{near}}|}{8\pi f_0}. \end{cases} \tag{16}$$

Due to the frequency-dependent magnetic materials core material having a very high permittivity [17], there is strong electric field coupling between the windings. Since the distance between the windings and the core is very close and the electric field coupling occurs through the equipotential core, the relative position of the two windings has a minimal effect on the parasitic capacitance between them. This has been verified in [27] and [34].

The equivalent circuit for the S_{21}^{IW} setup can be shown in Fig. 16(a). At low frequencies, the magnetic field response can be ignored, and the inductances in the figure can be considered short-circuited. The three parasitic capacitances C_{W} within the red box in Fig. 16(a) can be transformed using a star-delta transformation, resulting in the circuit shown in Fig. 16(b), which ultimately is equivalent to a capacitance with a value of $4C_{\mathrm{W}}$.

TABLE II
PARAMETERS OF THE CM MODEL CHARACTERIZING THE CMC OBTAINED THROUGH GA, AS SHOWN IN FIG. 9 OF THIS ARTICLE

	L_{C0}	C_{C0}	R_{C0}	C_{C}	L_{C2}	R_{C2}	L_{C3}	R_{C3}
Sample A	1.85 mH	300 pF	2900 Ω	42 pF	1.85 mH	3000 Ω	-	-
Sample B	1.1 mH	-	3500 Ω	30 pF	1 mH	500 Ω	10 mH	2000 Ω
Sample C	2 mH	240 pF	3000 Ω	55 pF	2 mH	3000 Ω	-	-

Therefore, the parasitic capacitance C_{W} between the windings can be obtained from the transmission coefficient S_{21}^{IW}

$$C_{\mathrm{w}} = \frac{1}{16\pi f_0 \sqrt{10^{\frac{40-S_{21}^{\mathrm{IW}}}{10}} - 10^4}}. \tag{17}$$

It is worth mentioning that the method proposed in this article successfully simplifies a complex structure into a simple *RLC* parallel structure. Only four different setups of $\mathrm{S_{21}}$ measurements and simple low-frequency and resonance point parameter extractions are needed, without requiring complex algorithms to extract DM parameters. This greatly reduces the complexity of the process and improves the accuracy of parameter extraction.

V. EXPERIMENTAL VALIDATION

Due to the numerous influencing factors in predicting the noise of the entire converter system, such as the parasitic capacitance of the switch to ground, parasitic parameters of the switches, parasitic parameters of the PCB, and ground impedance, it is challenging to directly simulate the converter system. Therefore, this article verifies the 4W-CMC model through insertion loss testing.

To validate the accuracy of the proposed model and parameter extraction method, several commercial 4W-CMCs were measured using an R&S ZND VNA. The results showed good fitting accuracy. This section presents the prediction results for three typical 4W-CMC models made from frequency-dependent magnetic materials. Most commercially available 4W-CMCs can be categorized as similar to these three samples. Sample A: IPE0-8 from Delta Electronics, removed from an EMI filter of an electric vehicle charger, featuring a manganese-zinc ferrite core. Sample B: SY4-50H103F09CV4L from Leesenworth, featuring a nanocrystalline core. Sample C: SY4-50H302M12CV4L from Leesenworth, featuring a manganese-zinc ferrite core. Unlike Sample C, Sample A is used in an OBC with bidirectional functionality, resulting in larger wire diameters for both windings, leading to increased asymmetry.

Table II lists the CM model parameters obtained via the GA algorithm for all CMCs analyzed in this section, while Table III provides the DM model parameters. For DM excitation of the dual-winding and quad-winding tests, a commercial 1:1 RF transformer (Coilcraft WB2010-SMLD) was used to assist the testing.

First, the fitting accuracy for sample A was validated. Figs. 17 and 18 show the response of sample A under CM excitation, measured using the S_{21}^{CM} setup in Fig. 5(a). The results indicate that this model can accurately fit the impedance trend of the

TABLE III
PARAMETERS USED TO CHARACTERIZE THE DM MODEL OF THE 4W-CMC IN FIG. 9 OF THIS ARTICLE

	L_D	C_D	R_D	M_{near}	M_{far}	C_W
Sample A	6.25 μH	4 pF	652 Ω	-0.8 μH	-4.25 μH	1.7 pF
Sample B	3.23 μH	10 pF	2150 Ω	-0.62 μH	-1.97 μH	0.27 pF
Sample C	5.73 μH	16 pF	4665 Ω	-1.36 μH	-3.56 μH	0.33 pF

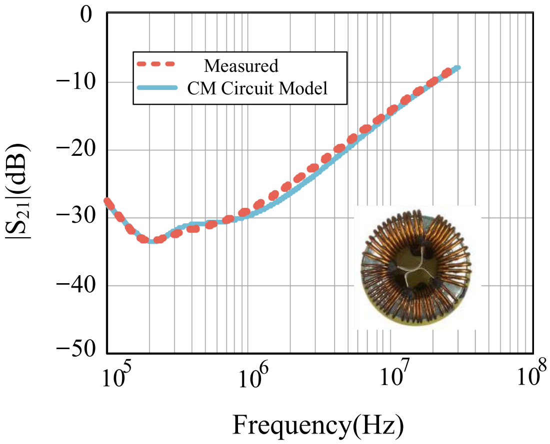

Fig. 17. Model fitting and measured S_{21} magnitude of Sample A under S_{21}^{CM} setup.

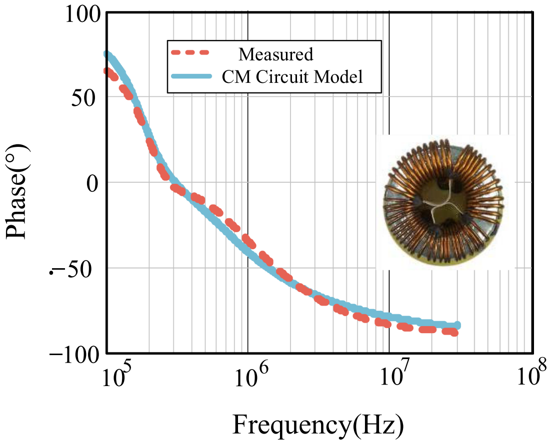

Fig. 18. Model fitting and measured S_{21} phase of Sample A under S_{21}^{CM} setup.

manganese-zinc ferrite CMC. Fig. 19 further verifies that the DM configuration for sample A under different windings can also accurately fit the DM response, effectively characterizing the different magnetic coupling characteristics of the 4W-CMC.

To further validate the applicability of the DM model, this article extends the testing frequency range for samples B and C to 50 MHz and compares the accuracy of the model with recent studies to demonstrate the advantages of the proposed method. Figs. 20 and 21 show the $|S_{21}|$ magnitude for samples B and C under the S_{21}^{CM} setup and compare them with the CM models of ferrite and nanocrystalline materials from [18] and [19]. Figs. 22 and 23 compare the $|S_{21}|$ phase for samples B and C under the S_{21}^{CM} setup. The CM parameters obtained from references [18] and [19] are listed in Table IV.

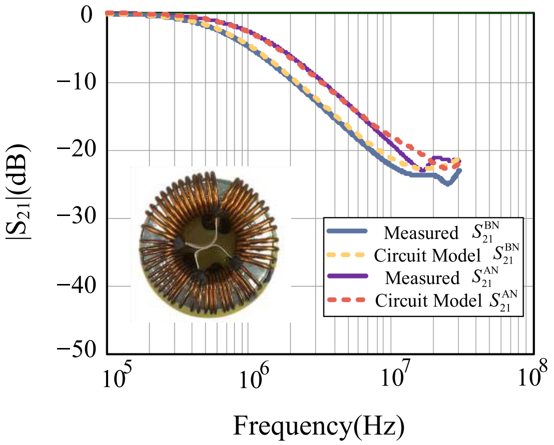

Fig. 19. Comparison of model fitting and measured S_{21} magnitude of Sample A under S_{21}^{ij} setup.

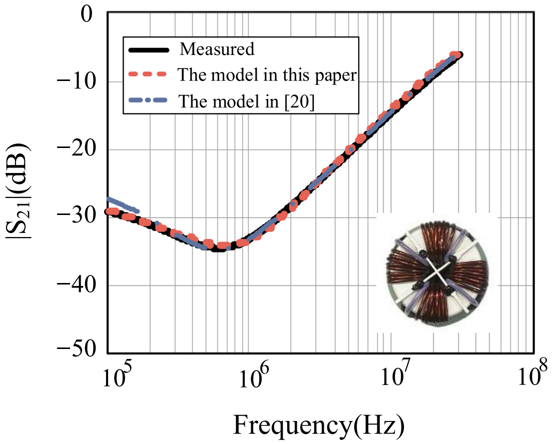

Fig. 20. Model fitting and measured S_{21} magnitude of Sample B under S_{21}^{CM} setup.

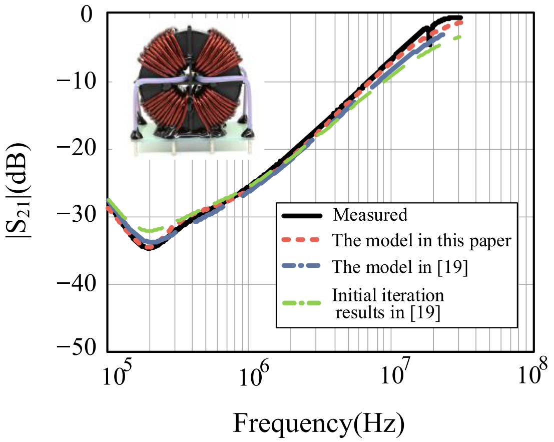

Fig. 21. Model fitting and measured S_{21} phase of Sample C under S_{21}^{CM} setup.

TABLE IV
CM COMPONENT MODEL PARAMETERS IN [18] AND [19]

	L_{C0}	R_{C0}	C_{C0}	L_{C1}/C_{C1}	R_{C1}	L_{C2}/C_{C2}	R_{C1}
Sample B	14 mH	6000 Ω	30 pF	5 mH	4000 Ω	18 mH	18k Ω
Sample C	3.4 mH	7000 Ω	65 pF	80 pF	6000 Ω	-	-

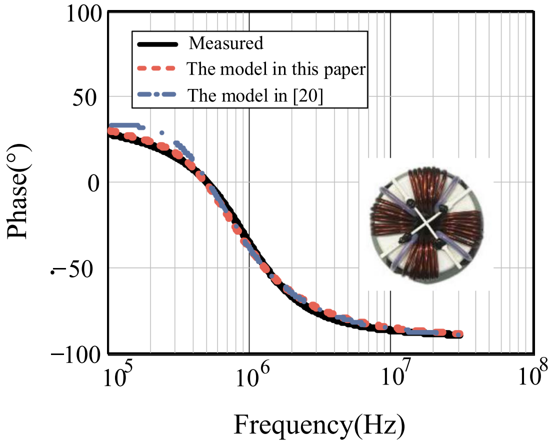

Fig. 22. Model fitting and measured S_{21} phase of Sample B under S_{21}^{CM} setup.

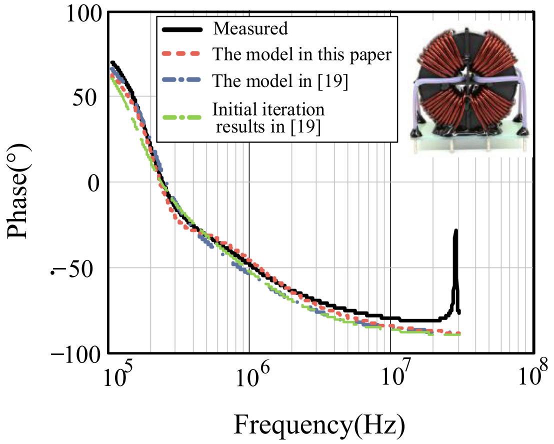

Fig. 23. Model fitting and measured S_{21} phase of Sample C under S_{21}^{CM} setup.

From Figs. 21 and 23, it can be observed that the model from [18] exhibits poorer accuracy compared to the model proposed in this article during the initial iterations. This may be due to the model lacking explicit initial values, causing the algorithm to become trapped in a local optimum. In contrast, the initial values for the model in this article are quite close to the results after iterations. When the particle velocity scaling factor and scaling factor to search away from the particle's best-known position in [18] were adjusted from 0.4 to 1.1 (which enhanced the search range of the PSO), the curve fitting became more accurate. This is because the CM model does not need to consider the coupling effects of the electric or magnetic fields between windings, fundamentally focusing on impedance modeling. Therefore, with sufficient order and well-tuned algorithm, good accuracy can be achieved. The model proposed in this article, due to the addition of the resonant capacitor C_{C0}, can provide a good fit for the ferrite CMC curves even in the initial fitting stage.

Figs. 22 and 24 show that this model can also be used for fitting nanocrystalline materials with C_{C0} set to zero, achieving comparable accuracy to the model in [19].

Figs. 24 and 25 show the attenuation performance of different windings of Sample B under DM excitation, while Figs. 26 and 27 show the attenuation performance of different windings of Sample C under DM excitation, compared with the method in [23] within 50 MHz. The DM parameters from the model in [23] are listed in Table V.

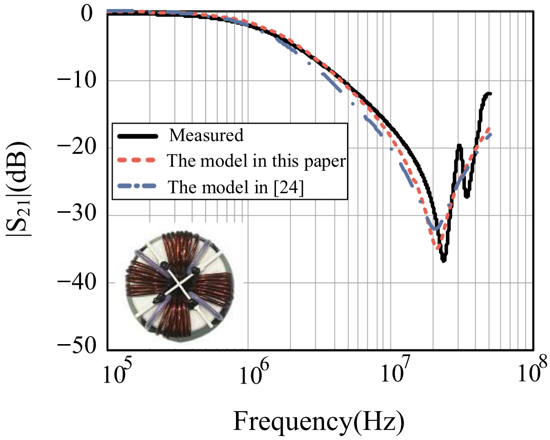

Fig. 24. Model fitting and measured S_{21} phase of Sample B under S_{21}^{AN} setup.

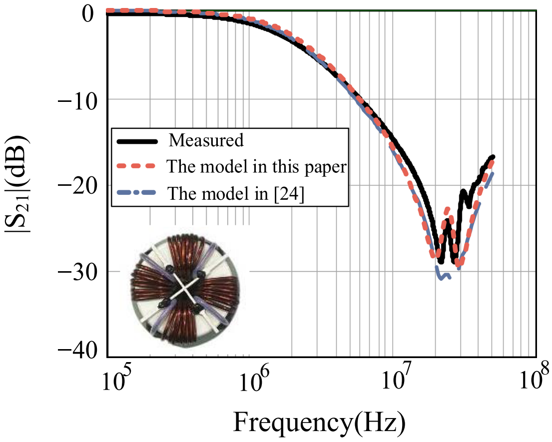

Fig. 25. Model fitting and measured S_{21} phase of Sample B under S_{21}^{BN} setup.

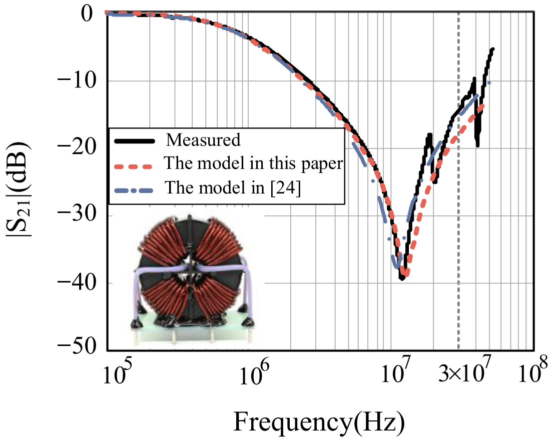

Fig. 26. Model fitting and measured S_{21} phase of Sample C under S_{21}^{AN} setup.

From the DM validation, it can be observed that the model proposed in this article shows good accuracy within the conducted EMI range up to 30 MHz. However, due to the appearance of new resonance points in the 30 MHz–50 MHz range, it becomes

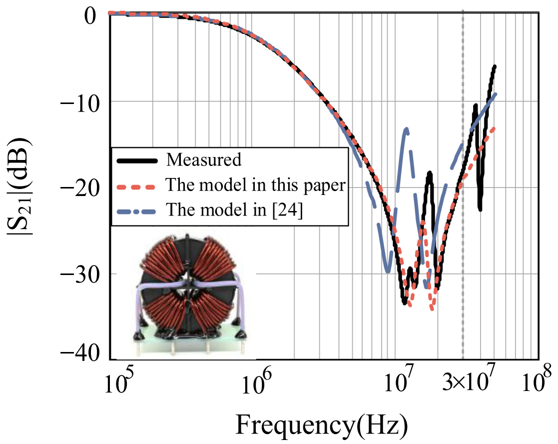

Fig. 27. Model fitting and measured S_{21} phase of Sample C under S_{21}^{BN} setup.

TABLE V
DM COMPONENT MODEL PARAMETERS IN [23]

	L_{D1}	L_{D2}	C_{D}	C_{W}	R_{D1}	R_{D2}
Sample B	4.8 nH	6.4 nH	11 pF	6 pF	3000 Ω	1835 Ω
Sample C	1.26 nH	1.1 nH	18 pF	3 pF	3600 Ω	3000 Ω

challenging to accurately fit the trend above 30 MHz. The model from [23] also demonstrates good accuracy under the S_{21}^{AN} setup, but after 10 MHz in the S_{21}^{BN} setup, it struggles to accurately fit the resonance points, suggesting that further adjustment of the PSO iteration parameters may be required. In conclusion, the CM and DM models proposed in this article exhibit good fitting accuracy within the conducted EMI range and simplify the modeling and parameter extraction process compared to existing models.

VI. CONCLUSION

Based on the analysis of the asymmetry and local symmetry of the 4W-CMC, this article proposes a novel high-frequency equivalent circuit model and parameter extraction procedure for frequency-dependent magnetic materials 4W-CMC. The key idea of the model lies in the CM model having clear physical significance, separating parasitic capacitance from capacitors that fit the nonlinear behavior of materials. The DM model accurately predicts the DM response in any connection, including the response to DM excitation in any two phases.

Parameter extraction of the CM model is based on an optimized parameter extraction procedure (GA) with relatively accurate initial value prediction. The parameter extraction of the DM model relies on insertion loss curves measured with different connection schemes, proposing a DM connection method specific to 4W-CMC, compared to traditional CMC and 3W-CMC connection schemes. This connection scheme, based on the local symmetry and mutual inductance cancellation mechanism of 4W-CMC, greatly simplifies the equivalent model. Compared to the latest research, the proposed model features fewer components to reduce model complexity and simplifies the parameter extraction process based on the newly introduced testing methods.

This article demonstrates the practical application of the model and parameter extraction method in modeling various industrial 4W-CMC. The generality of the method is validated through the use of different materials and 4W-CMC with asymmetric windings (different wire diameters per phase). Experimental results show very good consistency between the measured and model curves, and the fitting accuracy is effectively improved compared to the latest research.

REFERENCES

[1] Y. Zhou, W. Chen, and X. Yang, "Investigation of cascade connection method to improve the insertion loss of DM active EMI filters," *IEEE J. Emerg. Sel. Topics Power Electron.*, vol. 10, no. 1, pp. 1084–1094, Feb. 2022.

[2] Y. Han, Z. Wu, and D. Wu, "Hybrid common-mode EMI filter design for electric vehicle traction inverters," *Chin. J. Electric Eng.*, vol. 8, no. 4, pp. 52–60, Dec. 2022.

[3] M. Kumar and J. Kalaiselvi, "Analysis and measurement of non-intrinsic differential-mode noise in a SiC inverter fed drive and its attenuation using a passive sinusoidal output EMI filter," *IEEE Trans. Energy Convers.*, vol. 38, no. 1, pp. 428–438, Mar. 2023.

[4] L. Zhai, G. Hu, C. Song, M. Lv, and X. Zhang, "Comparison of two filter design methods for conducted EMI suppression of PMSM drive system for electric vehicle," *IEEE Trans. Veh Technol.*, vol. 70, no. 7, pp. 6472–6484, Jul. 2021.

[5] C. Domínguez-Palacios, P. González-Vizuete, M. A. Martín-Prats, and J. B. Mendez, "Smart shielding techniques for common mode chokes in EMI filters," *IEEE Trans. Electro Compat.*, vol. 61, no. 4, pp. 1329–1336, Aug. 2019,.

[6] A. Mallik, W. Ding, and A. Khaligh, "A comprehensive design approach to an EMI filter for a 6-kW three-phase boost power factor correction rectifier in avionics vehicular systems," *IEEE Trans. Veh Technol.*, vol. 66, no. 4, pp. 2942–2951, Apr. 2017.

[7] L. Fang, D. Boroyevich, P. Mattevelli, and N. Gazel, "A comprehensive design for high power density common mode EMI inductor," in *Proc. IEEE Energy Convers. Congr. Expo.*, Phoenix, AZ. USA., 2011, pp. 1861–1867.

[8] B. Touré, J.-L. Schanen, L. Gerbaud, T. Meynard, J. Roudet, and R. Ruelland, "EMC modeling of drives for aircraft applications: Modeling process, EMI filter optimization, and technological choice," *IEEE Trans. Power Electron.*, vol. 28, no. 3, pp. 1145–1156, Mar. 2013.

[9] H. Zhu, D. Liu, H. Chen, and G. Chen, "An improved foster model of common-mode inductor and its application in EMI filter design," in *Proc. IEEE Int. Symp. Electromagn. Compat. IEEE Asia-Pacific Symp. Electromagn. Compat.*, Suntec City, Singapore, 2018, pp. 461–465.

[10] K. Nomura et al., "Novel SPICE model for common mode choke including complex permeability," in *Proc. IEEE Appl. Power Electron. Conf. Expo.*, 2016, pp. 3146–3152.

[11] N. Moonen, R. Vogt-Ardatjew, A. Roc'h, and F. Leferink, "3-D full-wave high frequency common mode choke modeling," *IEEE Trans. Electro Compat.*, vol. 62, no. 3, pp. 707–714, Jun. 2020.

[12] A. Bingler, B. Pintér, K. Marák, S. Bilicz, and M. Csörnyei, "Surrogate model-based parameter identification for 3-D modeling of common mode chokes," *IEEE Trans. Magn.*, vol. 60, no. 3, Mar. 2024, Art. no. 8400604.

[13] M. L. Heldwein, L. Dalessandro, and J. W. Kolar, "The three-phase common-mode inductor: Modeling and design issues," *IEEE Trans. Ind Electron.*, vol. 58, no. 8, pp. 3264–3274, Aug. 2011.

[14] Q. Li, B. Xie, Y. Zhang, J. Ma, and C. Yuan, "A general analytical model of single-layer common-mode chokes," *IEEE Trans. Power Electron.*, vol. 39, no. 6, pp. 6591–6596, Jun. 2024.

[15] H. Jie et al., "VNA-based fixture adapters for wideband accurate impedance extraction of single-phase EMI filtering chokes," *IEEE Trans. Ind Electron.*, vol. 70, no. 8, pp. 7821–7831, Aug. 2023.

[16] P. Hu et al., "A simple measurement method for frequency-dependent impedance and parasitic parameters of common-mode chokes," in *Proc. IEEE Int. Symp. Electromagn. Compat., Signal Power Integrity*, New Orleans. LA. USA., 2019, pp. 266–271.

[17] A. Roc'h and F. Leferink, "Nanocrystalline core material for high performance common mode inductors," *IEEE Trans. Electro Compat.*, vol. 54, no. 4, pp. 785–791, Aug. 2012.
[18] Á. Ojeda-Rodríguez, J. Bernal-Méndez, and M. A. Martín-Prats, "Modal theory and approach for accurate characterization of common-mode chokes," *IEEE Trans. Power Electron.*, vol. 38, no. 9, pp. 10516–10529, Sep. 2023.
[19] A. Ojeda-Rodríguez, C. Dominguez-Palacíos, J. Bernal-Méndez, and M. A. Martín-Prats, "Simple and accurate characterization of nanocrystalline common mode chokes," in *Proc. IEEE Int. Symp. Electromagn. Compat. Signal/Power Integrity*, Spokane. WA. USA., 2022, pp. 472–477.
[20] J.-L. Kotny, X. Margueron, and N. Idir, "High-frequency model of the coupled inductors used in EMI filters," *IEEE Trans. Power Electron.*, vol. 27, no. 6, pp. 2805–2812, Jun. 2012.
[21] W. Tan, C. Cuellar, X. Margueron, and N. Idir, "A high frequency equivalent circuit and parameter extraction procedure for common mode choke in the EMI filter," *IEEE Trans. Power Electron.*, vol. 28, no. 3, pp. 1157–1166, Mar. 2013.
[22] I. Stevanovic, S. Skibin, M. Masti, and M. Laitinen, "Behavioral modeling of chokes for EMI simulations in power electronics," *IEEE Trans. Power Electron.*, vol. 28, no. 2, pp. 695–705, Feb. 2013.
[23] Á. Ojeda-Rodríguez, C. Domínguez-Palacios, J. Bernal-Méndez, and M. A. Martín-Prats, "Analyzing and characterizing common mode chokes for three phase systems," *IEEE Trans. Power Electron.*, vol. 39, no. 5, pp. 4916–4932, May 2024.
[24] Y. Lan, X. Zeng, W. Chen, and Q. Chen, " High-frequency model of common-mode choke in electromagnetic interference filters," in *Proc. Trans. China Electrotechnical Soc.*, Jun. 2024, pp. 1–11, doi: 10.19595/j.cnki.1000-6753.tces.240297.
[25] C. Domínguez-Palacios, J. Bernal, and M. M. Prats, "Characterization of common mode chokes at high frequencies with simple measurements," *IEEE Trans. Power Electron.*, vol. 33, no. 5, pp. 3975–3987, May 2018.
[26] C. Domínguez-Palacios, J. B. Mendez, and M. A. M. Prats, "Characterization of three-phase common-mode chokes at high frequencies," *IEEE Trans. Power Electron.*, vol. 33, no. 8, pp. 6471–6475, Aug. 2018.
[27] H. Jie et al., "High-precision broadband impedance measurements of three-phase common-mode chokes using single-port circuit de-embedding and three-port network calibration methods," *IEEE Trans. Ind Electron.*, vol. 71, no. 8, pp. 8248–8258, Aug. 2024.
[28] P. S. Niklaus, M. M. Antivachis, D. Bortis, and J. W. Kolar, "Analysis of the influence of measurement circuit asymmetries on three-phase CM/DM conducted EMI separation," *IEEE Trans. Power Electron.*, vol. 36, no. 4, pp. 4066–4080, Apr. 2021.
[29] P. S. Niklaus, D. Bortis, and J. W. Kolar, "Design and experimental analysis of a three-phase active CM/DM conducted EMI noise separator," *CPSS Trans. Power Electron Appl.*, vol. 5, no. 3, pp. 273–288, Sep. 2020.
[30] H. Hizarci, U. Pekperlak, and U. Arifoglu, "Conducted emission suppression using an EMI filter for grid-tied three-phase/level T-type solar inverter," *IEEE Access*, vol. 9, pp. 67417–67431, 2021.
[31] S. Wang, Y. Y. Maillet, F. Wang, R. Lai, F. Luo, and D. Boroyevich, "Parasitic effects of grounding paths on common-mode EMI filter's performance in power electronics systems," *IEEE Trans. Ind Electron.*, vol. 57, no. 9, pp. 3050–3059, Sep. 2010.
[32] W. Xu, Z. Zhao, and Q. Jiang, "Calculation method for parasitic capacitance of high-frequency transformers," *J. Tsinghua Univ. (Sci. Technol.).*, vol. 61, no. 10, pp. 1088–1096, Jul. 2021.
[33] S. W. Pasko, M. K. Kazimierczuk, and B. Grzesik, "Self-capacitance of coupled toroidal inductors for EMI filters," *IEEE Trans. Electromagn. Compat.*, vol. 57, no. 2, pp. 216–223, Apr. 2015.
[34] S. Li, S. Lu, and C. C. Mi, "Revolution of electric vehicle charging technologies accelerated by wide bandgap devices," *Proc. IEEE*, vol. 109, no. 6, pp. 985–1003, Jun. 2021.

Yujie Lan (Student Member, IEEE) was born in Fujian, China, in 1998. He received the B.S. degree in electrical engineering and automation from the Harbin University of Science and Technology, Harbin, China, in 2021. He is currently working toward the Ph.D. degree in power electronics and power drives with Fuzhou University, Fuzhou, China.

His research interests include high-frequency magnetic technology, electromagnetic compatibility diagnosis and suppression technology.

Wei Chen (Member, IEEE) received the M.S. and Ph.D. degrees in electrical engineering from Fuzhou University, Fuzhou, China, in 1987 and 1990, respectively.

He was a Senior Visiting Professor with the Center for Power Electronics Systems, Virginia Tech, Blacksburg, VA, USA, from 1996 to 1998. He was a Research and Development Manager with Delta Electronics Company Ltd., and the Delta Power Electronics Center, Shanghai, China, from 1999 to 2008. He has authored or coauthored more than 80 technical articles, including IEEE Transactions and Proceedings. He held more than 40 approved patents from China and USA. His research interests include power conversion, high-frequency magnetic technology, EMI debug and solution, wireless power transfer, electromagnetic field analysis, and applications.

Dr. Chen is a fellow of the Council of China Power Supply Society.

Qing He was born in Jiangxi, China, in 1999. He received the B.S. degree in electrical engineering and automation from the Tiangong University, Tianjin, China, in 2022. He is currently working toward the master's degree in power electronics and power drives with Fuzhou University, Fuzhou, China.

His research interest includes high frequency magnetic technology.

Qingbin Chen was born in Quanzhou, China. He received the B.E. and Ph.D. degrees in electrical engineering from Fuzhou University, Fuzhou, China, in 2007 and 2012, respectively.

He was a visiting scholar with the University of Florida, Florida, USA, from 2017 to 2018. His research interests include high frequency magnetic technology, EMC diagnosis and suppression technology, and wireless power transfer.

Dr. Chen is the member of Magnetic Components and Ferrite Materials (Magnetic Standards Committee of China) and served as the Vice chairperson and Deputy Secretary General of Magnetic Component Specialty Committee of CPSS.